Programmable Moving Defect for Spatiotemporal Wave Localization in Piezoelectric Metamaterials

Renan L. Thomes,[1,*] Danilo Beli,[2,†] Christopher Sugino,[3,‡] Alper Erturk,[1,§] and Carlos De Marqui Junior[2,¶]

[1] *G. W. Woodruff School of Mechanical Engineering, Georgia Institute of Technology, Atlanta, Georgia 30332, USA*

[2] *Department of Aeronautical Engineering, Sao Carlos School of Engineering, University of Sao Paulo (USP), Sao Carlos/SP 13566-590, Brazil*

[3] *Department of Mechanical Engineering, Stevens Institute of Technology, Hoboken, New Jersey 07030, USA*

(Received 22 September 2022; revised 16 February 2023; accepted 14 March 2023; published 9 June 2023)

In this work, we experimentally demonstrate the concept of space-time wave localization using programmable defects. The dynamic properties of the local resonators of an electromechanical metamaterial, comprising piezoelectric elements connected to synthetic impedance circuits, are digitally controlled to modulate a trivial point defect in space and time. The experimental results show that the vibration energy is gradually transferred and localized over subsequent unit cells according to the defect position. The practical realization of space-time wave localization using programmable defects in elastic metamaterials may enable innovative solutions for information transmission, multiplexing and demultiplexing, sensing, and coding.

DOI: 10.1103/PhysRevApplied.19.064031

I. INTRODUCTION

Phononic crystals and metamaterials are engineered structures capable of manipulating waves through band gaps, i.e., frequency bands where wave propagation is prohibited [1–3]. While the former is based on the destructive superposition of reflected and incident waves [4], the latter relies on energy absorption by an array of resonating units [5]. They have been used in several applications in the realm of acoustic and elastic waves such as isolation [6–9], cloaking [10], focusing [11], and guiding [12]. In particular, wave localization and guiding through fixed point and line defects in a periodic array of unit cells have received notable attention in the past two decades [13–15]. Specifically in metamaterials, trivial defects can be generated by introducing a mismatch in the dynamic properties of the selected resonators [16]. This periodicity breaking produces a defect wave state lying within the locally resonant band gap, which results in localized waves around a point defect or in propagating waves along a line defect [17,18].

The recent rise of programmable architected materials in which the unit cell properties change with time has expanded the wave manipulation possibilities [19,20]. For instance, these active media [21] have been used to tune band gaps in different frequencies [22,23], to create parametric amplification [24], to convert waves [25], as well as to design nonreciprocal [26] or topological pumping waveguides [27,28], which are phenomena related to space and/or time-reversal symmetry breaking [29,30]. These architected materials have also been used to create devices with reconfigurable defects [31–33].

Recently, Thomes *et al.* [34] expanded the possibilities of programmable wave localization by introducing the concept of space-time-varying defects to transmit and localize waves at specific locations of metamaterials. The authors numerically demonstrated that programming defects in a periodic array of electromechanical local resonators [35,36] through a smooth modulation strategy, as illustrated in Fig. 1, leads to energy transmission and space-time wave localization. In this work, we explore the experimental realization of such wave and dynamic phenomenon in a fully programmable and digitally reconfigurable piezoelectric metamaterial beam, opening possibilities for practical applications in fields such as information transmission [37], multiplexing and demultiplexing [38], sensing [39], and coding [40], among others.

*rthomes3@gatech.edu
†beli.danilo@gmail.com
‡csugino@stevens.edu
§alper.erturk@me.gatech.edu
¶demarqui@sc.usp.br

II. SPATIOTEMPORAL LOCAL RESONANCE TUNING

We consider a piezoelectric (or electromechanical) metamaterial beam, which has a substrate made of 6061

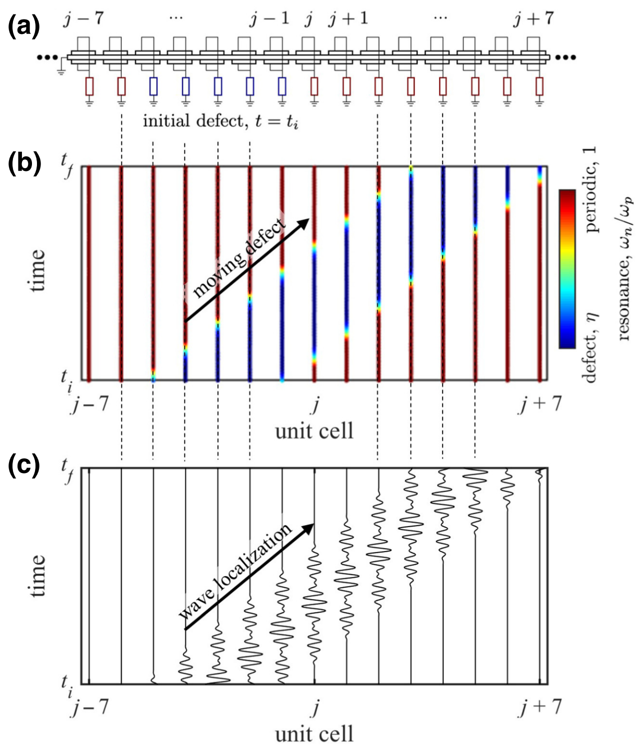

FIG. 1. Theoretical concept of the space-time defect modulation using a piezoelectric metamaterial beam. The wave localization (c) follows the defect position (b), which moves by smoothly modulating the dynamic properties of the shunt circuits, i.e., local resonators (a). Hence, the vibration energy originally concentrated around the initial defect (t_i) is progressively transferred to subsequent unit cells as the defect travels in space and time.

aluminum with cross section $b \times h = 10 \times 0.8128$ mm^2 and total length $L = 318$ mm. An array of 31 pairs of piezoelectric elements (size $b_p \times l_p \times h_p = 10 \times 10 \times 0.31$ mm^3 and model APC 850), separated by 0.25 mm from each other, brackets the substructure. Each piezoelectric element is covered by thin and conductive metallic electrodes on the top and bottom surfaces. The substrate and the internal electrodes are electrically grounded, while the external electrodes of each unit cell are connected in parallel and shunted through a synthetic impedance circuit, which has a digital filter in the loop such that its properties can be modified via computational software. Each synthetic circuit is designed as a voltage-controlled current source with the effective admittance in the Laplace domain (see Sugino *et al.* [20] for a detailed description of the synthetic circuit implementation) given by

$$Y(s) = \frac{I(s)}{V_{\text{in}}(s)} = \frac{V_{\text{out}}(s)}{V_{\text{in}}(s)\, R_c} = \frac{F(s)}{R_c}, \qquad (1)$$

where s is the Laplace parameter, $I(s)$ is the current supplied to the terminals of the piezoelectric patches, $V_{\text{in}}(s)$ is the piezoelectric voltage, R_c is a resistance for voltage-current conversion, and V_{out} is the output voltage, which depends on a selected transfer function $F(s) = V_{\text{out}}(s)/V_{\text{in}}(s) = R_c\, Y(s)$. In order to create an electromechanical local resonator, the admittance of the electrical circuit at unit cell j is written as

$$Y_j(s) = C_{p_j}\left(\frac{\omega_{n_j}^2}{s} + 2\xi_j\,\omega_{n_j}\right), \qquad (2)$$

where C_p is the piezoelectric capacitance, ω_n is the resonant frequency of the RLC circuit, and ξ is the electrical damping ratio.

To create the active domain, and hence to induce the spatiotemporal wave localization, the resonant frequency and the correspondent damping ratio of the synthetic impedances are simultaneously modulated in space (unit cell j) and time (t), respectively, by

$$\frac{\omega_{n_j}(t)}{\omega_p} = 1 - (1-\eta)\bar{\mathcal{H}} \quad \text{and} \quad \frac{\xi_j}{\xi_p}(t) = 1 - (1-\gamma)\bar{\mathcal{H}}, \qquad (3)$$

where ω_p and ξ_p are, respectively, the resonant frequency and the damping ratio of the periodic configuration; η and γ are, respectively, the constants that determine the frequency detuning and the damping ratio detuning of a shunt. In addition,

$$\bar{\mathcal{H}} = \left[H(j - j_f - \phi(t) + \delta) - H(j - j_l - \phi(t) - \delta)\right], \qquad (4)$$

where $H(x) = 0.5 + 0.5\tanh(\psi\, x)$ is an analytic approximation of the Heaviside step function for which $\psi = 5$ determines the sharpness of the step, j_f and j_l are, respectively, the indices of the first and last defected unit cells at $t = 0$, and $\delta = 0.3892$ is a constant to properly set the defect configuration to cells j_f until j_l ($H(\delta) = 0.98$). Notice that the defect position is determined by the H functions. The phase shift provided by $\phi(t) = (\Delta j/\Delta t)(t - t_i)$ gradually moves the defect to the right-hand side by Δj piezos in a time interval of $\Delta t = t_f - t_i$, where t_f and t_i are the final and initial times of the modulation (note that Eq. (3) is only valid for $t_i \le t \le t_f$). Instead of using the set of cosine functions combined to conditional clauses originally proposed by Thomes *et al.* [34], the modulation proposed here is more concise, provides an analogy to waves propagating with a phase velocity $\Delta j/\Delta t$, and is more easily programmed in a computational environment. However, both modulation strategies are analogous from the wave and dynamic points of view.

The digital implementation of the synthetic circuits enforces the time sampling of Eqs. (3) and (4), which transforms the continuous-time (t) to the discrete-time (t_k) domain. For the same reason, Eqs. (1) and (2) are represented in discrete-time analogue (z) instead of the Laplace parameter.

III. EXPERIMENTAL SETUP

The programmable experimental setup follows from Alshaqaq *et al.* [41,42] and Sugino *et al.* [43], previously used for concepts such as group velocity tailoring and nonreciprocal behavior. A schematic of the experimental setup is depicted in Fig. 2. The desired circuit parameters $\omega_{n_j}(t_k)$ and $\xi_j(t_k)$, and hence the electromechanical local resonator tuning, are digitally programmed through LabVIEW® software [Fig. 2(i)]. The correspondent discrete transfer functions $F(z)$ are calculated and uploaded into the controller, which uses a field-programmable gate array (FPGA) to control the transfer function of each shunt circuit in real time. Based on $F(z)$, the NI PXIe-1082 controller [Fig. 2(d)] calculates the output voltage $v_{\rm out}(t_k)$ that emulates the electrical circuit in each piezoelectric patch. More details of the design of such digital circuits are presented in Sugino *et al.* [20]. To implement time modulation of the effective impedance of each shunt circuit, the synthetic-impedance controller accepts a trigger signal input and updates the impedance setting on each rising edge of the trigger. During experiments, a signal generator [Fig. 2(g)] outputs a square burst signal as the trigger input to the controller, and the signal generator is in turn synchronized with the excitation to the system. In this way, the modulation of the shunt impedances is consistent between measurements, and the onset of modulation is synchronized with the excitation. The number of modulation steps is chosen to ensure that the state of the system at the end of the modulation is the same as the initial state. See Appendix A for more details regarding the digital parameters used in the experiments. Moreover, due to the time delay introduced by digital sampling (i.e. phase lag) [20,44], the unit cell with defect is tuned to lower frequencies compared with the periodic configuration ($\eta < 1$), where a smaller electrical damping is required to preserve the digital circuit stability when compared with the high-frequency tuning [20].

The metastructure with 31 unit cells ($j = [0\text{–}30]$) is clamped at $j = 0$ and free at $j = 30$ as presented in Fig. 2(b). The excitation signal is generated (and recorded) by a Polytec PSV-500 system [Fig. 2(f)] and amplified [Fig. 2(a)] before it reaches the piezoelectric patch terminals at position $j = 15$, which is exclusively used for actuation. The transverse velocity field is measured by a scanning laser Doppler vibrometer [Fig. 2(c)] at 93 points uniformly distributed along the metastructure. The velocity measurements for each point are carried out with five averages.

IV. EXPERIMENTAL RESULTS

A. Fixed defect

First, the periodic configuration (i.e., without defects), where the piezoelectric patches are shunted through synthetic-impedance circuits with $\omega_{n_{[0-30]}}/(2\pi) = \omega_p/(2\pi) = 4$ kHz and $\xi_{[0\text{–}30]} = \xi_p = 0.067$, is investigated. The excitation is a burst random signal. The frequency response function (FRF) averaged along the metastructure length is displayed in Fig. 3(a) (blue line) and shows a vibration attenuation zone around 4000–4240 Hz due to the locally resonant band gap of the shunt circuit. Next, a configuration with a fixed defect between unit cells 13 to 17 is created by tuning the corresponding shunt circuits to a different resonant frequency, $\omega_{n_{[13-17]}}/(2\pi) = 2$ kHz ($\eta = 0.5$). The damping ratio of those resonators is also reduced, $\xi_{[13\text{–}17]} = 0.0335$ ($\gamma = 0.5$), to maximize

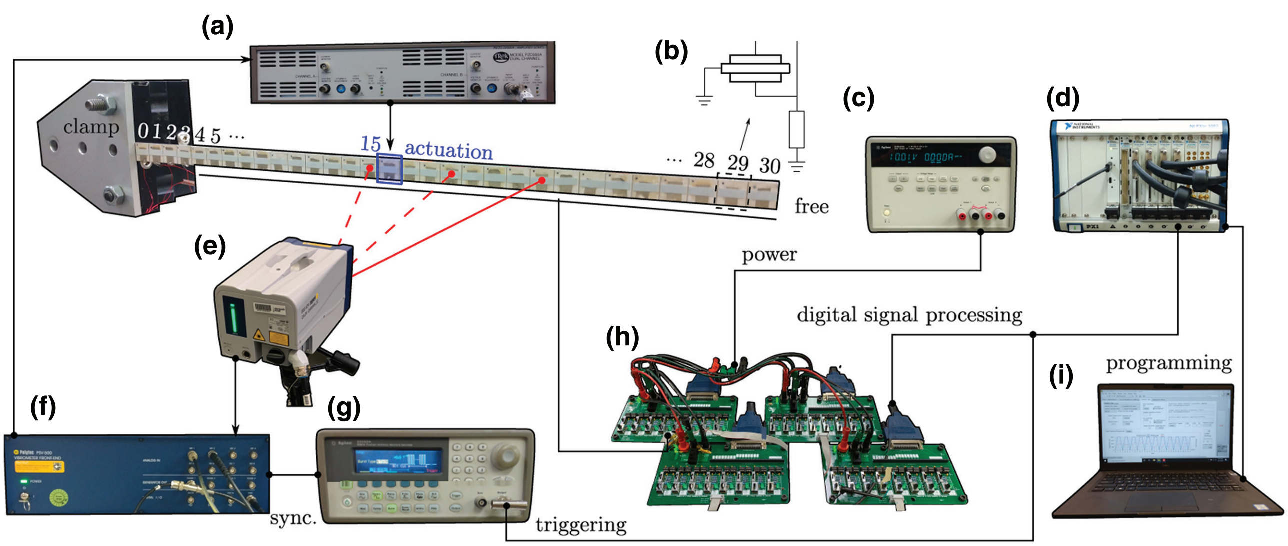

FIG. 2. Details of the experimental setup: (a) amplifier, (b) metastructure and unit cell, (c) power supply, (d) NI PXIe-1082 controller, (e) scanning laser Doppler vibrometer, (f) PSV-500 acquisition and signal input system, (g) signal generator, (h) printed circuit boards with the synthetic-impedance circuit for each piezoelectric pair, and (i) laptop with LabVIEW® software.

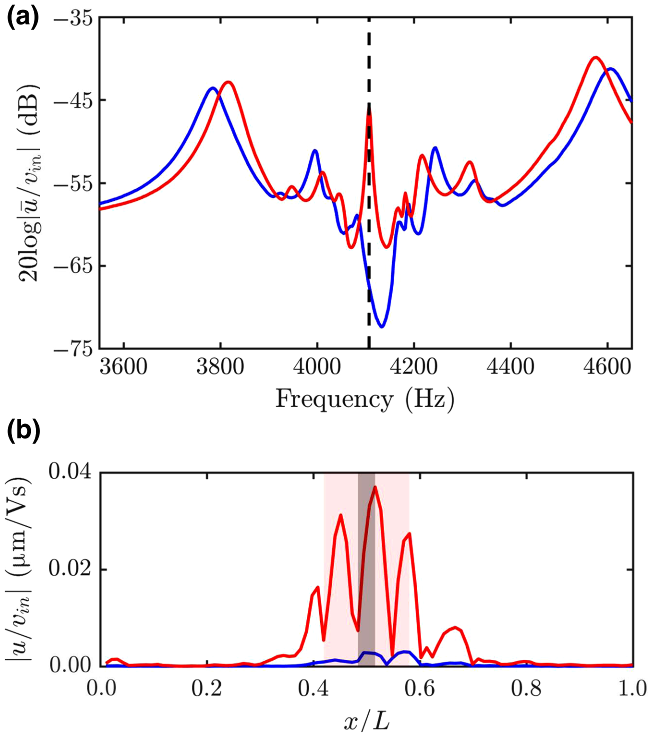

FIG. 3. (a) FRF averaged along the metastructure length and (b) velocity field at 4107.5 Hz, which is indicated by the black dashed line in (a): periodic (blue) and with defect (red). The FRF is computed by $20\log_{10}|\overline{u}/v_{\rm in}|$ (dB, reference 1 mm/V s), where $\overline{u}$ is the averaged velocity of the transverse motion and $v_{\rm in}$ is the input voltage. The red and gray shaded areas in (b) indicate, respectively, the defect and excitation zones.

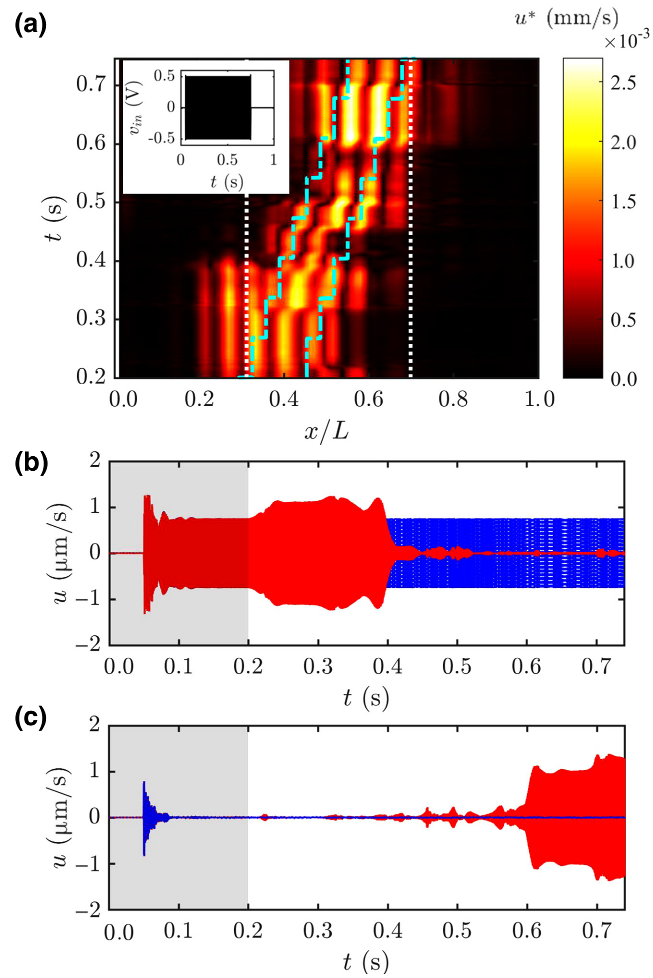

FIG. 4. (a) Envelope of the vibration field during the space-time modulation for continuous excitation. The cyan dashed lines indicate the defect position and the inset shows the excitation signal. (b),(c) Response for the fixed-defect (blue) and moving-defect (red) cases at selected positions indicated by the white dashed lines in (a). The gray shaded area indicates the interval before the onset of modulation.

the vibration amplitude of the defect mode. For the same burst random excitation, the frequency response of the metastructure with defect has a resonant peak inside the attenuation band (at 4107.5 Hz) due to the defect mode as presented in Fig. 3(a) (red line). In addition, the velocity field measured at the defect frequency for both configurations, shown in Fig. 3(b), highlight the high level of the spatial vibration localization around the defect when it is compared with the periodic configuration. Therefore, the vibration energy of the excitation is confined within the defect (red line), and the remaining periodic cells to the left and to the right of the defect work like domain wall protection [45].

B. Moving defect with continuous excitation

In order to experimentally observe the space-time modulation, the piezoelectric metastructure is continuously excited with a sine burst signal with central frequency of 4107.5 Hz [i.e., the defect frequency in Fig. 3(a)]. The defect is initially placed at unit cells 9 to 13 and then moved 8 cells towards the right-hand side, i.e., to $j = [17–21]$. The space-time modulation starts at $t_i = 0.2$ s, after the beam vibration reaches the steady-state regime. See Appendix A for the updated time modulation parameters. The envelope of the time-domain velocity response (u^*) along the metastructure is plotted in Fig. 4(a) with the position of the defect boundaries defined by the cyan dashed lines [obtained from Eq. (3)]. As expected, the vibration pattern related to the defect mode presented in Fig. 3(b) moves towards the right-hand side of the metastructure following the space-time-modulated defect. Since the excitation at the piezoelectric patch placed at $j = 15$ is similar to a fixed defect (i.e., the piezoelectric patch responsible by the excitation is not shunted like the other unit cells), the defect mode pattern slightly changes when the moving defect includes this unit cell.

To highlight the previous spatiotemporal wave localization phenomenon, the time responses of the space-time-modulated defect case are compared with the fixed-defect case (i.e., $j = [9–13]$). Figures 4(b) and 4(c) display, respectively, the transverse velocity measured at unit cells $j = 13$ and $j = 21$, which corresponds to the positions $x/L = 0.312$ and $x/L = 0.699$ highlighted by the white dotted lines in Fig. 4(a). Both cases reach the steady-state regime before $t = 0.2$ s, when the space-time modulation starts for the moving-defect case. As predicted by the harmonic response in Fig. 3, the time response for the fixed defect (blue line) presents a constant and high vibration amplitude within the defect [Fig. 4(b)] and low vibration amplitude outside the defect [Fig. 4(c)]. This behavior occurs because the unit cells $j \in [14, 21]$ have a band gap at the excitation frequency, which does not allow the vibration transmission from $j = 15$ to $j = 21$ and works as a domain wall for the wave localization within the defect. On the other hand, the time responses for the spatiotemporal defect case (red line) are in agreement with the defect position. Initially, the vibration amplitude at $j = 13$ [Fig. 4(b)] is similar to the one observed at the steady-state regime, and then it decreases to almost zero as the defect moves further way. The opposite occurs in Fig. 4(b) where, initially, the vibration level at $j = 21$ is almost zero and it reaches the steady-state regime level when the spatiotemporal defect is transferred to this unit cell. This experiment confirms the theoretically predicted space-time wave localization by programming defects in a periodic array of electromechanical resonators [34] and clearly shows its flexibility in relation to the fixed-defect case.

C. Moving defect with transient excitation

The energy transfer through subsequent unit cells in the active metastructure is also experimentally observed by using a transient excitation. Again, the space-time modulation starts after the steady-state regime is reached. However, in this case, no external energy (i.e., excitation) is added to the system during the modulation of the resonators, except for the voltage supplied to the digital circuits by the controller. The time parameters are adjusted (see Appendix A) to produce a narrow-band excitation at the defect frequency and to obtain a reasonable vibration level after the end of the excitation at 0.5 s. The defect is initially placed at unit cells 13 to 17 and moved two cells forward when the modulation starts at 0.523 s. Moreover, due to the intrinsic damping in the system, the vibration response rapidly decays without an external energy input. Therefore, to observe the space-time wave localization with transient excitation, a faster modulation transition is programmed.

Figure 5(a) displays the envelope of the time-domain velocity responses (u^*) along the metastructure. The vibration energy (and, hence, the wave localization) has been moved towards the free end of the metastructure following the defect position indicated by the cyan dashed lines. Differently from the continuous-excitation responses of Fig. 4,

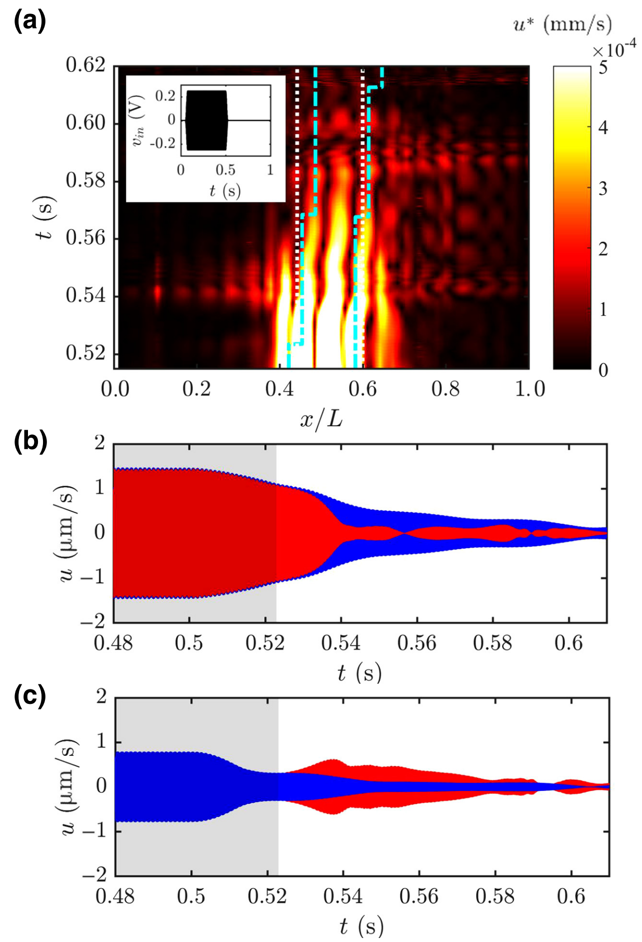

FIG. 5. (a) Envelope of the vibration field during the space-time modulation for transient excitation. The cyan dashed lines indicate the defect position and the inset shows the excitation signal. (b),(c) Response for the fixed-defect (blue) and moving-defect (red) cases at selected positions indicated by the white dashed lines in (a). The gray shaded area indicates the interval before the onset of modulation.

the vibration amplitude related to defect mode is attenuated over time due to the intrinsic damping.

To better understand this spatiotemporal localization under transient excitation, as well as the effects of damping and moving energy on the vibration amplitude, Figs. 5(b) and 5(c) present the time responses at $j = 13$ ($x/L = 0.442$) and $j = 18$ ($x/L = 0.600$) for the moving-defect and fixed-defect (at $j = [13–17]$) cases. As expected, the responses match until the onset of the modulation ($t = 0.523$ s). When the external excitation is removed ($t = 0.5$ s), the vibration response for the fixed defect (blue line) gradually decays in time within the defect [Fig. 5(b)] as well as at its neighboring unit cell [Fig. 5(c)]. This fixed-defect case captures only the damping contributions on the vibration response, which is used as a reference for the spatiotemporal defect case. For the moving-defect case, the amplitude of the time response at $j = 13$ [red line in

Fig. 5(b)] decays faster than in the fixed-defect case, highlighting the effects of wave (and vibration energy) manipulation in space and time due to programmable defects. Furthermore, Fig. 5(c) shows that the vibration amplitude at $j = 18$ increases after the onset of the modulation, indicating that energy has been transferred to this unit cell, which is later dissipated due to damping effects. Therefore, the energy transfer and the higher vibration amplitude for longer periods (compared with the fixed-defect case) are due to the space-time modulation of the defect. Despite the attenuation in the time response, this experimental observation also proves the feasibility of the space-time wave localization and energy transfer between subsequent unit cells using the defect modulation with a transient time excitation.

V. CONCLUSIONS

In conclusion, the presented results provide the experimental observation of the space-time wave localization in an electromechanical metamaterial beam by programmable defects. Notwithstanding the limitations imposed by the intrinsic damping, this space-time modulation can be implemented to systems where damping does not play a major role in the dynamic response, such as in acoustics and photonics. Even so, the insights and concepts demonstrated herein for both continuous or transient excitation may open avenues for practical implementations of programmable wave localization in mechanical and aerospace structures as well as wave devices.

ACKNOWLEDGMENTS

D.B. and C.D.M. gratefully acknowledge the support from Sao Paulo Research Foundation (FAPESP) through Grants No. 2018/18774-6 and No. 2018/15894-0 as well as the National Council for Scientific and Technological Development (CNPq) through Grants No. 433456/2018-3 and No. 308690/2019-2. R.L.T. and A.E. acknowledge support from the Woodruff Professorship and Carl Ring Family Chair endowments.

APPENDIX: ADDITIONAL INFORMATION ON THE TIME DISCRETIZATION AND FPGA MEMORY LIMITATION

Although Eqs. (3) and (4) are defined continuously in time, the digital implementation enforces a time discretization dictated by the update rate of the controller, f_{up} (Hz), so that $t_{k+1} - t_k = 1/f_{\text{up}}$, where k is the time-step index. Consequently, the total time of the modulation is given by

$$\Delta t = (n_Y - 1)/f_{\text{up}}, \tag{A1}$$

where n_Y is the total number of impedance values assigned to a shunt circuit. The performance of the modulation is determined by two qualities: speed and sharpness. While the former relates to $\partial\omega_n/\partial t \propto \Delta j/\Delta t$ and should be slow enough to avoid parametric excitation [34,46], the latter is exclusively related to the discrete nature of the problem and is proportional to $|\Delta\omega_{n_j}|/\omega_p = |\omega_n(j, t_{k+1}) - \omega_n(j, t_k)|/\omega_p = (1 - \eta)/(n_Y - 1)$. As $|\Delta\omega_{n_j}|/\omega_p$ increases, the change in the circuit parameters from one time step to another becomes more abrupt, and the modulation dissociates from a smooth and continuous function in time. Typically, n_Y is chosen to be as large as possible given the limitations of the FPGA memory, which in our case is $n_Y = 901$, and f_{up} is selected to have a desired Δt. For the harmonic response (Fig. 3) with fixed defect, an acquisition rate of 8 kHz and a frequency resolution $\Delta f = 2.5$ Hz are used. For the continuous-time excitation (Fig. 4), $f_{\text{up}} = 1.65$ kHz is used, which corresponds to $\Delta t = 0.546$ s. For the transient-time excitation (Fig. 5), a faster modulation is required due to the high intrinsic damping, and hence $f_{\text{up}} = 10$ kHz is used, which corresponds to $\Delta t = 0.09$ s.

[1] M. I. Hussein, M. J. Leamy, and M. Ruzzene, Dynamics of phononic materials and structures: Historical origins, recent progress, and future outlook, Appl. Mech. Rev. **66**, 040802 (2014).

[2] G. Ma and P. Sheng, Acoustic metamaterials: From local resonances to broad horizons, Sci. Adv. **2**, e1501595 (2016).

[3] S. A. Cummer, J. Christensen, and A. Alù, Controlling sound with acoustic metamaterials, Nat. Rev. Mater. **1**, 16001 (2016).

[4] M. Sigalas and E. Economou, Elastic and acoustic wave band structure, J. Sound Vib. **158**, 377 (1992).

[5] Z. Liu, X. Zhang, Y. Mao, Y. Y. Zhu, Z. Yang, C. T. Chan, and P. Sheng, Locally resonant sonic materials, Science **289**, 1734 (2000).

[6] J. V. Sánchez-Pérez, D. Caballero, R. Mártinez-Sala, C. Rubio, J. Sánchez-Dehesa, F. Meseguer, J. Llinares, and F. Gálvez, Sound Attenuation by a Two-Dimensional Array of Rigid Cylinders, Phys. Rev. Lett. **80**, 5325 (1998).

[7] K. M. Ho, C. K. Cheng, Z. Yang, X. X. Zhang, and P. Sheng, Broadband locally resonant sonic shields, Appl. Phys. Lett. **83**, 5566 (2003).

[8] O. R. Bilal and M. I. Hussein, Trampoline metamaterial: Local resonance enhancement by springboards, Appl. Phys. Lett. **103**, 111901 (2013).

[9] D. Beli, M. Ruzzene, and C. De Marqui Jr., Bridging-Coupling Phenomenon in Linear Elastic Metamaterials by Exploiting Locally Resonant Metachain Isomers, Phys. Rev. Appl. **14**, 034032 (2020).

[10] S. A. Cummer and D. Schurig, One path to acoustic cloaking, New J. Phys. **9**, 45 (2007).

[11] S. Guenneau, A. Movchan, G. Pétursson, and S. Anantha Ramakrishna, Acoustic metamaterials for sound focusing and confinement, New J. Phys. **9**, 399 (2007).

[12] M. Kafesaki, M. M. Sigalas, and N. García, Wave guides in two-dimensional elastic wave band-gap materials, Phys. B Condens. Matter **296**, 190 (2001).

[13] M. M. Sigalas, Defect states of acoustic waves in a two-dimensional lattice of solid cylinders, J. Appl. Phys. **84**, 3026 (1998).

[14] M. Torres, F. R. De Espinosa, G. P. García-Pablos, and N. García, Sonic Band Gaps in Finite Elastic Media: Surface States and Localization Phenomena in Linear and Point Defects, Phys. Rev. Lett. **82**, 3054 (1999).

[15] A. Khelif, A. Choujaa, B. Djafari-Rouhani, M. Wilm, S. Ballandras, and V. Laude, Trapping and guiding of acoustic waves by defect modes in a full-band-gap ultrasonic crystal, Phys. Rev. B **68**, 214301 (2003).

[16] N. Kaina, A. Causier, Y. Bourlier, M. Fink, T. Berthelot, and G. Lerosey, Slow waves in locally resonant metamaterials line defect waveguides, Sci. Rep. **7**, 15105 (2017).

[17] M. M. Sigalas, Elastic wave band gaps and defect states in two-dimensional composites, J. Acoust. Soc. Am. **101**, 1256 (1997).

[18] A. Shakeri, S. Darbari, and M. Moravvej-Farshi, Designing a tunable acoustic resonator based on defect modes, stimulated by selectively biased PZT rods in a 2D phononic crystal, Ultrasonics **92**, 8 (2019).

[19] M. Attarzadeh, J. Callanan, and M. Nouh, Experimental Observation of Nonreciprocal Waves in a Resonant Metamaterial Beam, Phys. Rev. Appl. **13**, 021001 (2020).

[20] C. Sugino, M. Ruzzene, and A. Erturk, Digitally Programmable Resonant Elastic Metamaterials, Phys. Rev. Appl. **13**, 061001 (2020).

[21] S. Xiao, T. Wang, T. Liu, C. Zhou, X. Jiang, and J. Zhang, Active metamaterials and metadevices: a review, J. Phys. D: Appl. Phys. **53**, 503002 (2020).

[22] V. Candido de Sousa, D. Tan, C. De Marqui, and A. Erturk, Tunable metamaterial beam with shape memory alloy resonators: Theory and experiment, Appl. Phys. Lett. **113**, 143502 (2018).

[23] T. M. P. Silva, M. A. Clementino, V. C. de Sousa, and C. De Marqui, An experimental study of a piezoelectric metastructure with adaptive resonant shunt circuits, IEEE ASME Trans. Mechatron. **25**, 1076 (2020).

[24] G. Trainiti, Y. Xia, J. Marconi, G. Cazzulani, A. Erturk, and M. Ruzzene, Time-Periodic Stiffness Modulation in Elastic Metamaterials for Selective Wave Filtering: Theory and Experiment, Phys. Rev. Lett. **122**, 124301 (2019).

[25] K. Yi, M. Collet, and S. Karkar, and Reflection and transmission of waves incident on time-space modulated media, Phys. Rev. B **98**, 054109 (2018).

[26] J. Marconi, E. Riva, M. Di Ronco, G. Cazzulani, F. Braghin, and M. Ruzzene, Experimental Observation of Nonreciprocal Band Gaps in a Space-Time-Modulated Beam Using a Shunted Piezoelectric Array, Phys. Rev. Appl. **13**, 031001 (2020).

[27] E. Riva, G. Castaldini, and F. Braghin, Adiabatic edge-to-edge transformations in time-modulated elastic lattices and non-hermitian shortcuts, New J. Phys. **23**, 093008 (2021).

[28] Y. Xia, E. Riva, M. I. N. Rosa, G. Cazzulani, A. Erturk, F. Braghin, and M. Ruzzene, Experimental Observation of Temporal Pumping in Electromechanical Waveguides, Phys. Rev. Lett. **126**, 095501 (2021).

[29] D. Beli, P. B. Silva, and J. R. de França Arruda, Mechanical circulator for elastic waves by using the nonreciprocity of flexible rotating rings, Mech. Syst. Signal Process. **98**, 1077 (2018).

[30] H. Nassar, B. Yousefzadeh, R. Fleury, M. Ruzzene, A. Alù, C. Daraio, A. N. Norris, G. Huang, and M. R. Haberman, Nonreciprocity in acoustic and elastic materials, Nat. Rev. Mater. **5**, 667 (2020).

[31] J. H. Oh, I. Kyu Lee, P. Sik Ma, and Y. Young Kim, Active wave-guiding of piezoelectric phononic crystals, Appl. Phys. Lett. **99**, 083505 (2011).

[32] Y.-F. Wang, T.-T. Wang, Y.-S. Wang, and V. Laude, Reconfigurable Phononic-Crystal Circuits Formed by Coupled Acoustoelastic Resonators, Phys. Rev. Appl. **8**, 014006 (2017).

[33] G. H. Li, Y. Z. Wang, and Y. S. Wang, Active control on switchable waveguide of elastic wave metamaterials with the 3D printing technology, Sci. Rep. **9**, 16226 (2019).

[34] R. L. Thomes, D. Beli, and C. De Marqui Jr., Space–time wave localization in electromechanical metamaterial beams with programmable defects, Mech. Syst. Signal Process. **167**, 108550 (2022).

[35] C. Sugino, S. Leadenham, M. Ruzzene, and A. Erturk, An investigation of electroelastic bandgap formation in locally resonant piezoelectric metastructures, Smart Mater. Struct. **26**, 055029 (2017).

[36] K. Yi and M. Collet, Broadening low-frequency bandgaps in locally resonant piezoelectric metamaterials by negative capacitance, J. Sound Vib. **493**, 115837 (2021).

[37] R. W. Ziolkowski, Superluminal transmission of information through an electromagnetic metamaterial, Phys. Rev. E **63**, 046604 (2001).

[38] Y. Pennec, B. Djafari-Rouhani, J. O. Vasseur, A. Khelif, and P. A. Deymier, Tunable filtering and demultiplexing in phononic crystals with hollow cylinders, Phys. Rev. E **69**, 046608 (2004).

[39] C. E. Zaki, A. Mehaney, H. M. Hassanein, and A. H. Aly, Fano resonance based defected 1d phononic crystal for highly sensitive gas sensing applications, Sci. Rep. **10**, 17979 (2020).

[40] J. Lan, Y. Liu, T. Wang, Y. Li, and X. Liu, Acoustic coding metamaterial based on non-uniform Mie resonators, Appl. Phys. Lett. **120**, 163501 (2022).

[41] M. Alshaqaq, C. Sugino, and A. Erturk, Programmable Rainbow Trapping and Band-Gap Enhancement via Spatial Group-Velocity Tailoring in Elastic Metamaterials, Phys. Rev. Appl. **17**, L021003 (2022).

[42] M. Alshaqaq, C. Sugino, and A. Erturk, in *Active and Passive Smart Structures and Integrated Systems XVI*, Vol. 12043, edited by J.-H. Han, S. Shahab, and J. Yang, International Society for Optics and Photonics (SPIE, 2022), p. 1204316.

[43] C. Sugino, M. Alshaqaq, and A. Erturk, Spatially programmable wave compression and signal enhancement in a piezoelectric metamaterial waveguide, Phys. Rev. B **106**, 174304 (2022).

[44] G. Raze, J. Dietrich, and G. Kerschen, Onset and stabilization of delay-induced instabilities in piezoelectric digital

vibration absorbers, J. Intell. Mater. Syst. Struct. **33**, 2033 (2022).

[45] S.-H. Jo, H. Yoon, Y. C. Shin, W. Choi, C.-S. Park, M. Kim, and B. D. Youn, Designing a phononic crystal with a defect for energy localization and harvesting: Supercell size and defect location, Int. J. Mech. Sci. **179**, 105670 (2020).

[46] A. Champneys, in *Encycl. Complex. Syst. Sci.*, edited by R. A. Meyers (Springer New York, New York, NY, 2009), p. 2323.